Geotechnical Engineering Journal of the SEAGS & AGSSEA Vol. 49 No. 2 June 2018 ISSN 0046-5828

Finite Element Analysis to Characterize the Lateral Behaviour of a Capped Pile Group

Chao-Kuang Hsueh[1], San-Shyan Lin[2] and Dominic E. L. Ong[3]

[1]*Assistant Professor, Department of Merchant Marine, National Taiwan Ocean University, Keelung, Taiwan.*

[2]*Professor, Department of Harbor and River Engineering, National Taiwan Ocean University, Keelung, Taiwan.*
Adjunct Professor, Swinburne University of Technology, Sarawak Campus, Malaysia.

[3]*Associate Professor, Swinburne University of Technology, Sarawak Campus, Malaysia.*

E-mail: sslin@mail.ntou.edu.tw

ABSTRACT: Finite element simulation for analysis of a capped pile group was conducted to investigate the interaction among piles, soil and pile cap, especially the effects resulted from concrete damaging. The simulation was to develop a calibrated model using the test data and to apply that model for conditions not present during the test. In addition to consider pile/soil and cap/pile interaction in the numerical simulation, interaction between steel reinforcement and concrete was also modelled in the analysis. Each steel reinforcement installed in the tested piles and the pile cap was modelled as an individual element at its installed position in the numerical analysis. The simulation results showed that the leading and the middle row piles in the group carried the highest and the lowest fraction of pile head loads when concrete around the pile cap/soil contact area remained its integrity. Increasing loading level, the pile head load carried by the middle row increased due to constraint of the pile cap affected by the concrete damage at the pile cap/soil contact zone.

KEYWORDS: Pile group, Lateral pile loading test, Finite element analysis, Concrete cracking, Soil-pile interaction.

1. INTRODUCTION

To provide enough capacity for lateral loading, a pile foundation is often designed in groups with a cap providing the connection between the structure and each single pile under the cap. Depending on the pile-to-cap embedment length and the amount of the provided reinforcement, the pile cap induces some degree of horizontal restraint at the top of the pile. Studies have found that resistance to a lateral loading is then provided by pile-soil-pile interaction, base and/or side friction along the concrete-soil interface (Rollins and Cole, 2006). Several studies on pile group performance have provided important insight into the behavior of pile-soil-pile interaction because of the stress overlapping caused reduction of overall capacity relative to that of a single pile (Muqtadir and Desai, 1986; Brown and Shie, 1990; Bhowmik, 1992; Yang and Jeremic, 2003; Comodromosa et al., 2009, and Lin et al., 2005 etc.). Previous works either neglected the nonlinear flexural behavior of pile or simplified the connection between pile head and cap as a fixed or a free boundary condition. The works by Mokwa and Duncan (2003), Rollins and Cole (2006) and Lin and Liao (2013) were available on cap-pile head interaction. Lemnitzer et al. (2010) focused on the nonlinear efficiency of bored pile group under lateral load. Relatively little information on effect of concrete damaging evaluated for large scale concrete pile group is reported in the literature.

A large-scale lateral loading test was conducted on two capped pile groups in Chiayi, Taiwan in 1997. The bored pile group consisted of six drilled shafts with diameter 1.5m, which was installed to a depth of 34.9m. The ratio of center to center spacing between piles over pile diameter was 3. The reinforced concrete pile cap was rectangular: 12m in length (L), 8.5m in width (W) and a thickness (D) of 2m. To have more understanding on the effect on concrete cracking on performance of a capped bored pile group subjected to lateral loading, the purpose of the study is to calibrate a model to the test data obtained from the pile group tested in Chiayi and to use the model to evaluate the interaction among pile, soil and pile cap. A model calibrated using the Chiayi test data for the free head single pile was studied by Hsueh et al. (2004). In this study, the 3D finite element software ABAQUS (Hibbit et al., 2002) is used for pile group simulation. The properties of soil, concrete and steel reinforcement are all modelled using nonlinear constitutive law. The installed steel reinforcement is modelled using a special individual element which can anchor at the interface node of the concrete element at exact the same location of the tested pile group.

2. BRIEF OF THE PILE GROUP TEST

A large scale lateral loading test of two pile groups were conducted at Chiayi, Taiwan. The arrangement of the test set up of the pile groups is shown in Figure 1. One of the pile groups consisted of six drilled shafts and the other group consisted of twelve driven precast concrete (PC) piles. The pre-stressed PC piles were circular and hollow cast in 17m long segments in the manufacture factory. In this paper, the study is only focusing on the drilled shaft group. The drilled shafts were installed by reverse circulation method. Reinforcing cage consists of fifty-two 32mm longitudinal reinforcement placed in a circular arrangement within each pile, with 16mm hoop steel bars used as circular ties.

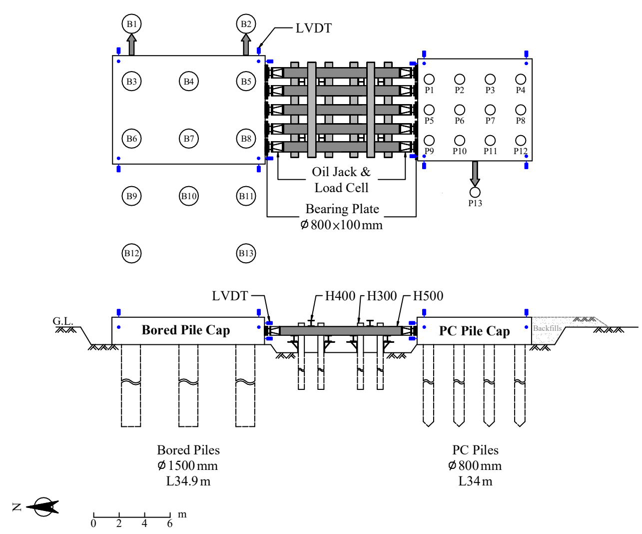

Figure 1 Arrangement of the test setup (Chen, 1997)

The bars extended 1.65m into each pile, leaving 1.35m bond length within the pile cap. Detail of the connection between pile head and pile cap is shown in Figure 2. The reinforced concrete cap was sitting on the excavated level ground surface. Inclinometer casings were attached to the longitudinal bars of the reinforcement cage. The inclinometer casings were extending to the full thickness of the pile cap. The ratio of center to center spacing between piles over pile diameter was 3 for both groups. Structural properties of the tested piles and typical soil properties of the testing site are given in Tables 1 and 2, respectively.

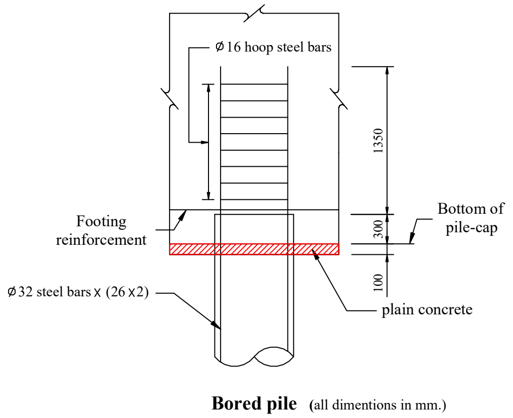

Figure 2 Detail of the reinforcement connection between pile head and cap (Chen, 1997)

Table 1 Structural properties of tested piles (Chen, 1997)

	Cross-Section (m^2)	Concrete				Steel		
		f_c' (MPa)	f_t' (MPa)	E_c (GPa)	ν_c	f_y (MPa)	E_{st} (GPa)	ν_{st}
B3 ~ B8	1.767	27.47	3.28	24.62	0.18	412.02	200.12	0.29
Cap	102							

Table 2 Site stratigraphy and soil conditions at the test site (Chen, 1997)

Depth (m)	SPT-N	Classification	γ_t (kN/m^3)	E_s (kPa)	c (kPa)	ϕ (°)	S_u (kPa)	ϕ' (°)	ν_s	K_o
0-3	1~5	ML/SM	18.64	44584	1.0	13.5	—	31.7	0.4	0.63
3-8	8~19	SM	18.64	49407	1.0	12	—	33.4	0.3	0.72
8-12	4~12	CL	18.69	81935	14.81	10.8	45.38	—	0.45	0.78
12-16	15~29	SM	18.84	96605	1.0	18.2	—	35	0.3	0.76
16-22	11~23	CL/SM	18.84	122379	1.0	16.8	—	33.3	0.4	0.68
22-32	9~27	CL	18.76	242855	19.6	21	64.41	—	0.45	0.6
32-40	14~45	SM	19.07	282625	1.0	25	—	41.5	0.3	0.55

Lateral loading tests on the two groups were conducted by push the two pile caps away from each other (Figure 1). Five pairs of 5MN hydraulic jacks and load cells were used for lateral force application. Detail information regarding testing of the pile group can be referred to Chen (1997), Brown et al. (2001), or Lin and Liao (2006).

3. BRIEF OF THE PILE GROUP TEST

3.1 Finite Element Modelling

A three dimensional finite element model created in ABAQUS (Hibbit et al., 2002) is used to simulate the tested pile group (see Figure 1) given in Figures 3 to 5. The shaft cross-section and the pile cap is modelled with 8-node solid element (C3D8). The longitudinal and hoop steel reinforcement are modelled using REBAR element in the software library. These elements in the software are anchored at the interface nodes of the concrete element.

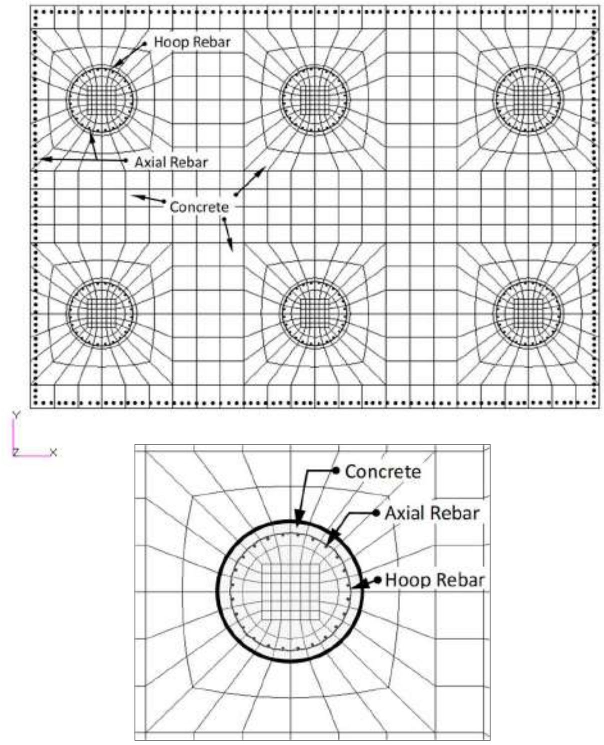

Figure 3 Detail of the steel reinforcement

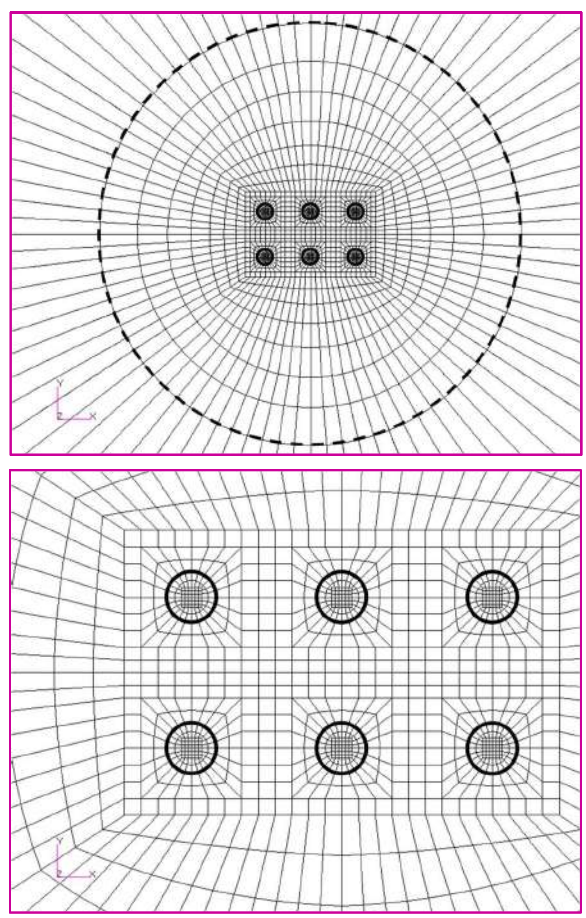

Figure 4 Plane view of the finite element mesh

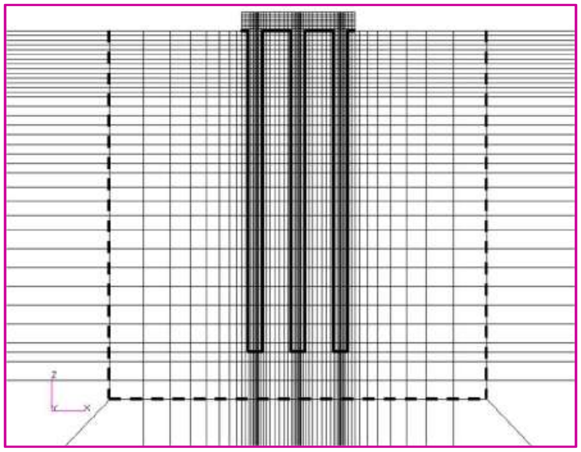

Figure 5 Elevation view of the finite element mesh

Each steel reinforcement is arranged at the exact location of the tested pile group. Plan and elevation view of the finite element mesh including soil boundary are shown in Figures 4 and 5, respectively. In the figures, the dark dash line is the boundary of the near and the far field soil. The infinite element (CIN3D8) was used in the far field to simulate the semi-infinite boundary. The soil domain in the near field is also modelled with 8-node solid element. The distance of the near field is assumed as ten times of the pile diameter. In addition, the dark solid line represents the interface between pile structure and soil. The function "CONTACT PAIR" in the software library is used to model the frictional contact for the shaft-soil interaction by assuming the master and slave surface as the shaft surface and soil, respectively.

3.2 Material Modelling

3.2.1 Concrete model

The uniaxial compressive stress-strain relationship given in Figure 6 is assumed to represent the behavior of concrete. In general, concrete tends to have linear and nonlinear behavior within and beyond 30% of the maximum compressive strength, respectively.

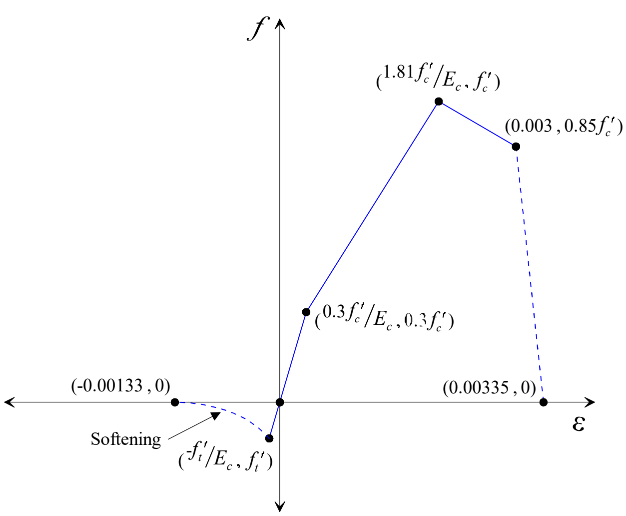

Figure 6 Uniaxial compressive stress-strain relationship of concrete (Hsueh et al., 2004)

After the maximum compressive strength is reached, concrete turns to behave softening and begins to crush. Furthermore, concrete tends to crack when the subjected tensile stress is larger than its tensile strength. Material properties used in the nonlinear analysis are given in the following:

Based on the ACI code (1995), elastic modulus of the concrete is given as:

$$E_c = 57000\sqrt{f_c'}\ (psi) \approx 4730\sqrt{f_c'}\ (MPa) \approx 15000\sqrt{f_c'}\ (kg/cm^2) \tag{1}$$

where f_c' is the peak strength of concrete.

In addition, based on the study by MacGregor (1988), the respective strain relevant to the maximum strength is:

$$\varepsilon_c = {}^{1.81f_c'}/_{E_c} \tag{2}$$

The ultimate tensile strength or the cracking failure stress of concrete is also adopted from the ACI code (1995) and is given as:

$$f_t = 7.5\sqrt{f_c'}\ (psi) \approx 2.0\sqrt{f_c'}\ (kg/cm^2) \tag{3}$$

With regard to the yield criterion of the concrete, assuming the material follows the associated flow rule, we have (Hibbit, 2002):

$$f_c = q - \sqrt{3}\, a_0\, p - \sqrt{3}\, \tau_c = 0 \tag{4}$$

where a_0 is a constant which is chosen from the ratio of the ultimate stress reached in biaxial compression to the ultimate stress reached in uniaxial compression, τ_c is the yield stress in a state of pure shear stress, and p is the effective stress and can be expressed as:

$$p = -\tfrac{1}{3}trace(\sigma) = -\tfrac{1}{3}\sigma : \mathrm{I} = -\tfrac{1}{3}(\sigma_x + \sigma_y + \sigma_z) = -\tfrac{I_1}{3} \tag{5}$$

in which σ is the stress tensor, I is the unit matrix, I_1 is the first invariant of the stress tensor, and following the definition of the Mises equivalent deviatoric stress, q is defined as:

$$q = \sqrt{\tfrac{3}{2}\, S : S} = \sqrt{\tfrac{3}{2}\, S_{ij}\, S_{ji}} = \sqrt{3 J_2} \tag{6}$$

where $S = \sigma + p\,\mathrm{I}$ are the deviatoric stress tensor components, and J_2 is the second invariant of the deviatoric stress tensor.

Once concrete crack occurs, the material stiffness needs to be adjusted to take into account the cracking effect. Whether concrete is cracked or not is evaluated at integration points of each element, based on the Coulomb line defined as:

$$f_t = \hat{q} - \left(3 - b_0 \tfrac{\sigma_t}{\sigma_t^u}\right)\hat{p} - \left(2 - \tfrac{b_0}{3}\tfrac{\sigma_t}{\sigma_t^u}\right)\sigma_t = 0 \tag{7}$$

where σ_t is the equivalent uniaxial tensile stress, σ_t^u is the failure stress in uniaxial tension, b_0 is a constant which is obtained from the value of the tensile failure stress in a state of biaxial stress when the other nonzero principal stress is at the uniaxial compression ultimate stress value, and $\hat{p}$ and $\hat{q}$ are defined in the same way as p and q in Eqs. (5) and (6), respectively, except that all stress components associated with open cracks (concrete cracking has occurred) are not included (Hibbit, 2002).

3.2.2 Steel model

Steel reinforcing bars are assumed to be elastic-plastic axially loaded elements. Discrete reinforcing bars are embedded within the solid element. The elastic-plastic model with strain hardening is considered in the steel reinforcement as shown Figure 7.

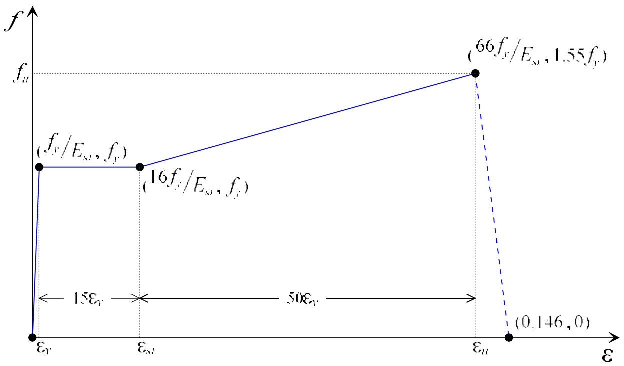

Figure 7 Stress-strain relationship of steel reinforcement (Hsueh et al., 2004)

The elastic modulus of steel rebar from the ACI code (1995) is given as:

$$E_s = 29 \times 10^6\ (psi) \approx 2.04 \times 10^6\ (kg/cm^2) = 200124\ (MPa) \tag{8}$$

3.2.3 Soil model

The conventional Mohr-Coulomb constitutive law with elastic-perfectly plastic behavior is used to model soil behavior. The required parameters are Mohr-Coulomb strength parameters for shear strength (i.e. cohesion c and friction angle ϕ) and elastic moduli as given in Table 2.

Brief review of the model is given in the following:

$$\tau = c + \sigma \tan \phi \tag{9}$$

where τ is the shear stress, σ is the normal stress, and ϕ is the angle of internal friction.

Based on the Mohr circle, we can obtain:

$$\tau = \frac{(\sigma_1 - \sigma_3)}{2} \cos \phi \tag{10}$$

and

$$\sigma = \frac{(\sigma_1 + \sigma_3)}{2} - \frac{(\sigma_1 - \sigma_3)}{2} \sin \phi \tag{11}$$

where σ_1 is the maximum principal stress, and σ_3 is the minor principal stress.

Substituting τ and σ into Eq. (9), we have:

$$\frac{(\sigma_1 - \sigma_3)}{2} - c \cos \phi - \frac{(\sigma_1 + \sigma_3)}{2} \sin \phi = 0 \tag{12}$$

3.3 Single Pile Analysis

Lateral test was firstly conducted on the B2 pile given in Figure 1. The cap of pile group was served as a reaction system. The calculated and the measured load deflection relationship at the pile head are shown in Figure 8 for comparison. Good agreement is obtained because nonlinear flexural stiffness of the piles was considered in the numerical analysis. The calculated deflection and the soil plastic strain zones around the shaft under maximum applied loading are shown in Figure 9. It also indicates the ground displacement at distance of 15m (about 10 times of shaft diameter) away from the shaft center, which is less than 1.5mm and its corresponding strain is only about 0.018%. In addition, the contour diagram of the soil plastic strain zone shows the soil yields within the distance of six times of shaft diameter. Since ground displacement at location of fifteen times of the shaft diameter from the shaft center approaches zero, hence the assumed boundary between near and far field is appropriate.

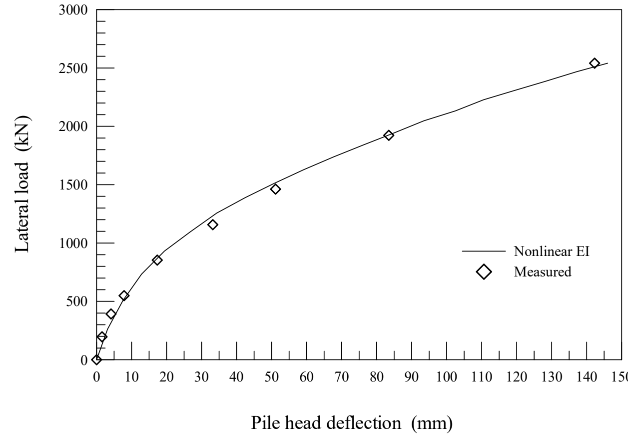

Figure 8 Load deflection curve at pile head

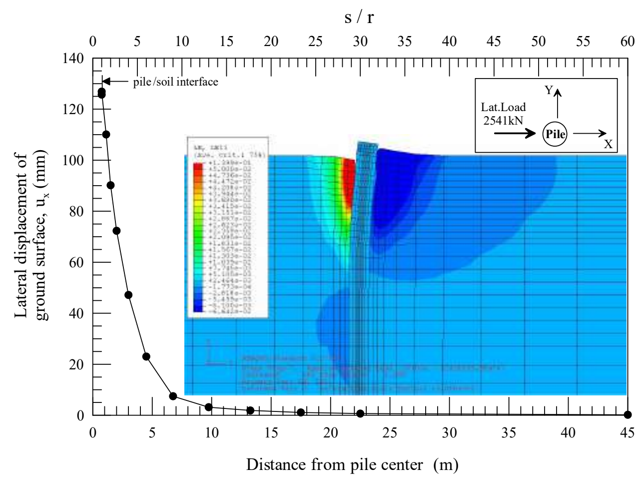

Figure 9 Calculated lateral displacement of ground and pile

The calculated and the measured deflection, moment, shear, soil resistance profile and rebar stress along shaft are given in Figures 10 and 11, respectively. When the applied loading level reaches 2,541kN, the rebar stress at the tension side has reached its yield strength of the reinforcement. The maximum rebar stress occurred at 7m below the ground surface.

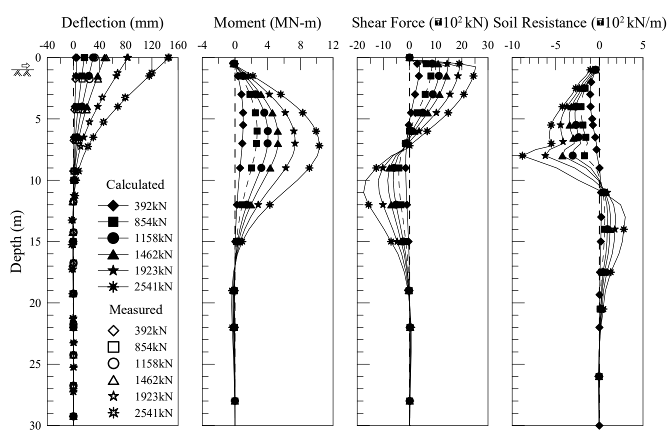

Figure 10 Comparison between calculated and measured deflection, moment, shear, and soil resistance profile

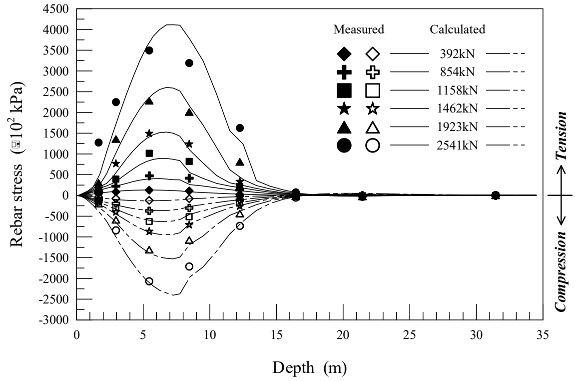

Figure 11 Comparison between calculated and measured rebar stress

In addition, effect of concrete crack pattern on the moment-curvature relationship is given in Figure 12. Based on these calculated results, we can see that pile shaft rigidity is significantly affected by the concrete cracking pattern along shaft. The calculated shaft cracking moment is about 1,700kN-m, which matches the tested shaft material and geometric properties. When lateral load increased to 854kN, the bending moments of the shaft at depth 3m to 9m exceeded their cracking moment, resulting in some local concrete cracking in the shaft. The concrete cracking effect is more severe and spread up- and downward when the applied lateral loading increased, as shown in Figure 12.

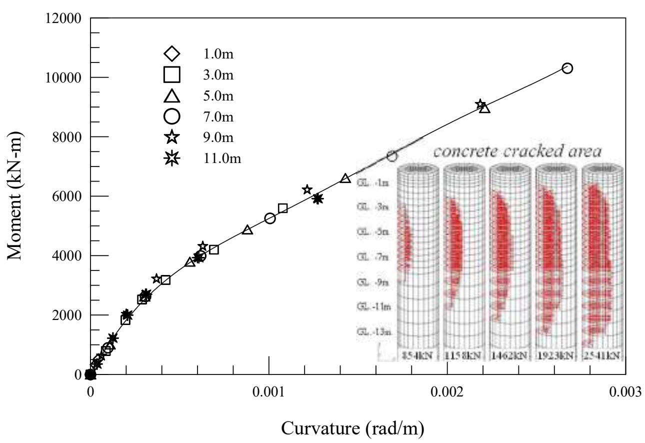

Figure 12 Moment curvature relationship

3.4 Pile Group Analysis

The load-deflection response at the pile cap is nonlinear as shown in Figure 13, in which the measured results based on two different tests are also given for comparison. Reasonable agreement is observed between the calculated and measured results. The first test for this case was a virgin loading, which was stopped when the PC-pile group was observed too weak when applied lateral load reached the level of 6,112kN. The second test was carried out with lateral load increased to 10,948kN, after placement of backfill behind the PC-pile group.

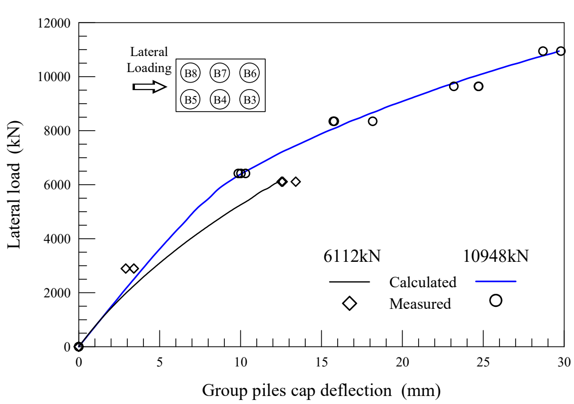

Figure 13 Load deflection curve at pile cap

Figures 14 and 15 present the simulated displacement of the pile cap, piles and ground under maximum applied loading.

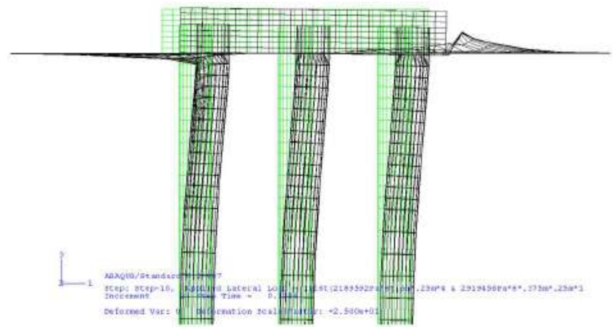

Figure 14 Simulated lateral displacement of the pile group and ground surface

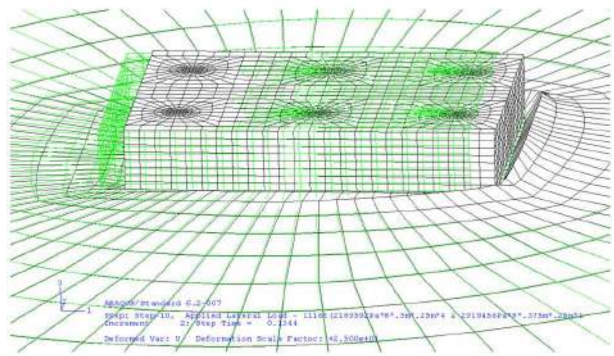

Figure 15 Simulated lateral displacement at the pile cap/soil contact area

As shown in the figures, the pile cap appears to have a clockwise rotation of degree 0.03°, which caused 36.9mm uplifting of the ground in front of the pile cap. These calculated values coincide with the observed results during the test. The simulated lateral displacement of the ground surface at the pile cap/soil contact area under maximum applied loading is shown in Figure 16, it showed that the ground surface affected by the lateral load reached out to the far field either in front of the pile cap or behind the pile cap.

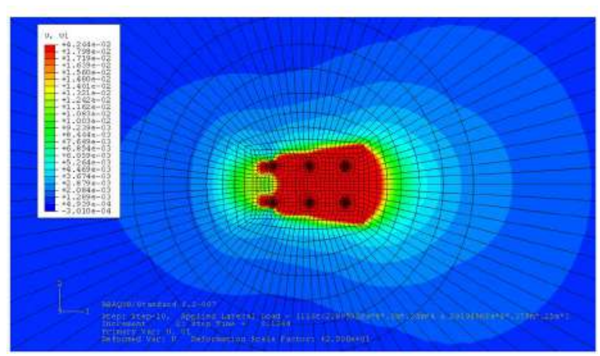

Figure 16 Plan view of simulated lateral displacement

Elevation view of the simulated ground lateral displacement given in Figure 17 showed the disturbed area is deeper than that of a single pile with free head given in Figure 9. Separation between the pile cap and the ground behind the trailing row piles was also observed as shown in the figure.

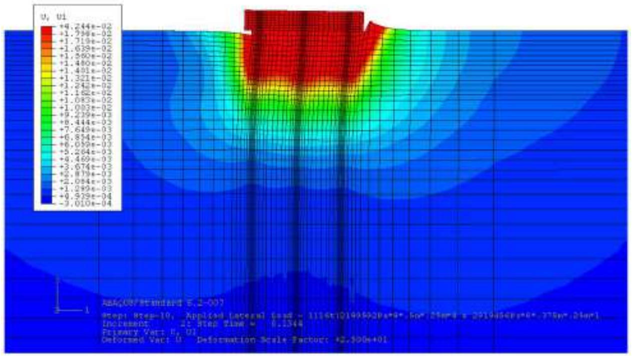

Figure 17 Elevation view of simulated lateral displacement

Figures 18 and 19 showed the plan view and elevation view of the simulated plastic strain distribution under the maximum applied loading. The yield zone at the ground surface in front of the pile cap was extended to a distance four times the shaft diameter. In addition, localized plastic strain zone was also observed behind the trailing row piles as shown in these figures. Behind the trailing row piles, it was observed that the plastic strain extended down to a depth about 7m below the pile cap.

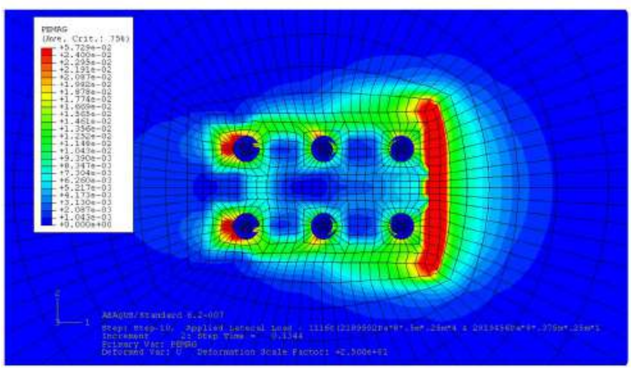

Figure 18 Plan view of simulated plastic strain under the maximum applied loading

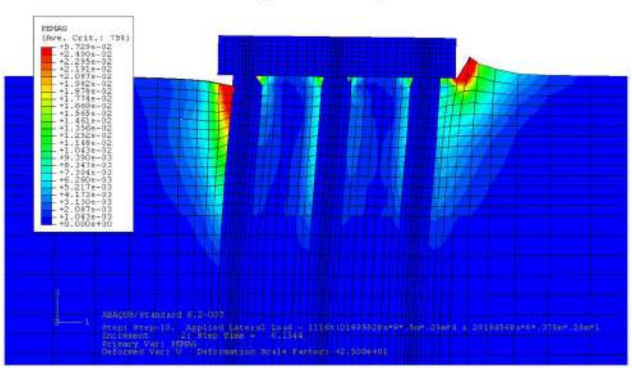

Figure 19 Elevation view of simulated plastic strain under the maximum applied load

Table 3 gives the calculated values of the load carried at the pile head of the piles on each row and the base shear below the pile cap. In the table, Stol represents the level of total lateral load applied at the pile cap. Based on the table, the contribution of the pile cap base shear frictional resistance was 3.5%. In addition, the leading, middle and trailing row piles carried 34.4%, 30.6% and 31.4%, respectively, of the total applied load at the pile cap.

Table 3 Ratio of load carried by each row of piles

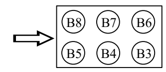

Load (S_{tol}, kN)	B5&B8 Avg. (S_{58}, kN)	B5&B8 S_{58} / S_{tol}	B4&B7 Avg. (S_{47}, kN)	B4&B7 S_{47} / S_{tol}	B3&B6 Avg. (S_{36}, kN)	B3&B6 S_{36} / S_{tol}	Cap Friction (F, kN)	Cap F / S_{tol}
2894	465.1	0.161	438.5	0.152	492.1	0.170	102.6	0.035
6112	966.6	0.158	940.9	0.154	1063.6	0.174	169.4	0.028
6416	1022.7	0.159	968.6	0.151	1092.1	0.170	249.0	0.039
8348	1310.0	0.157	1273.7	0.153	1438.1	0.172	304.7	0.037
9643	1498.5	0.155	1486.0	0.154	1669.3	0.173	335.7	0.035
10948	1676.5	0.153	1705.5	0.156	1907.6	0.174	386.7	0.034
Avg.	-	**0.157**	-	**0.153**	-	**0.172**	-	**0.035**

The data given in Table 3 can be re-drawn in Figure 20, in which the S_{avg} is the applied lateral force at the pile cap divided by the total numbers of pile. The leading and the middle row piles in the group carried the highest and the lowest load when the concrete at the pile cap/soil contact area remained its integrity. Increasing the applied loading until concrete cracked, the release of cap constraint due to cracked concrete caused increasing of load carried by the middle row. In general, the load carried by the leading row and the middle row increases with increasing of applied lateral load. On the contrary, the trailing row and the pile cap base friction decreases with increasing of applied load. In addition, both Figures 20 and 21 were also shown that the load carried by the leading row piles was higher than that of the S_{avg} during the whole applied loads.

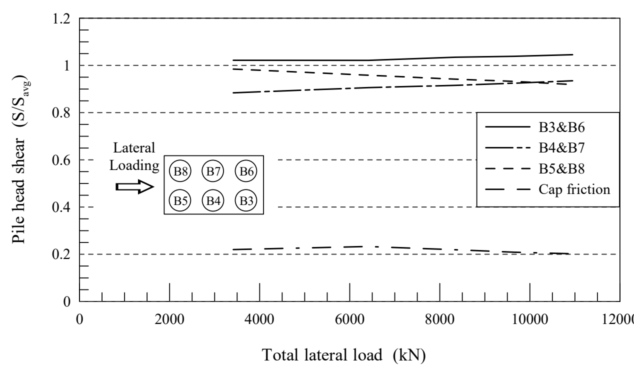

Figure 20 Ratio of shear force carried by each row of piles

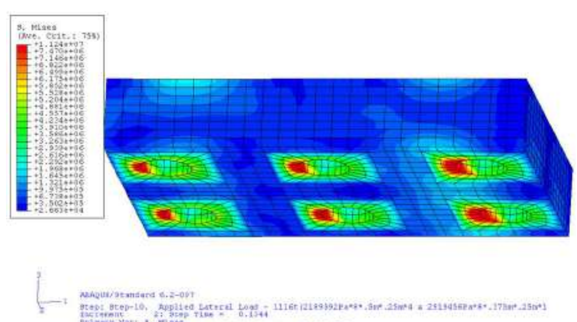

Figure 21 Simulated pile head stress below the pile cap under the maximum applied loading

Figure 22 presents the profiles of deflection, moment, shear force and soil lateral resistance of the piles B3 to B8 under the maximum applied loading. The measured inclinometer data is also provided for comparison. The maximum moment occurs at a depth of 8m below ground surface.

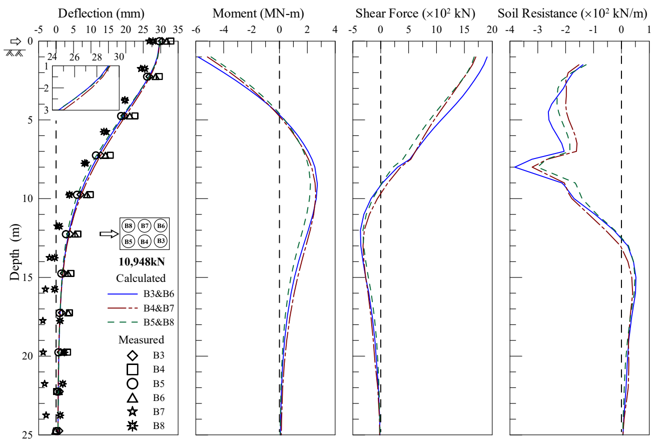

Figure 22 Deflection, moment, shear, and soil resistance profile

In addition, as shown in the figure, the piles in the leading row and the middle row have the lowest and the highest lateral deflection below the pile cap. The soil resistance profile showed that the highest resistance occurred near the maximum moment location. The maximum and the minimum soil resistance also occur at leading row and trailing row, respectively. At top 4m below ground surface, the highest soil resistance was observed at the leading row piles.

Predicted pile cap concrete crack pattern under the maximum applied lateral loading level is shown in Figure 23. It's shown concrete cracking was severe in trailing row piles but moderate in leading rows. As shown in Figure 13, the last step loading level of the first test was 6,112kN, which already caused the moment in the pile section higher than that of the crack moment of 1,554kN-m.

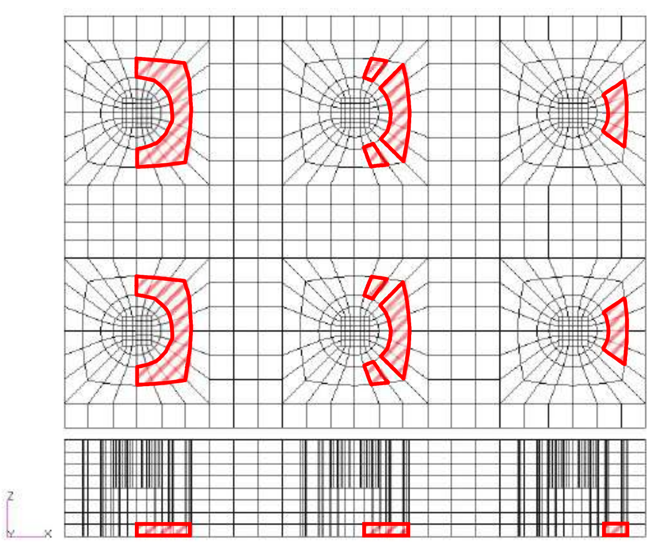

Figure 23 Plan view of the pile cap cracked concrete pattern

The predicted concrete crack pattern along shaft is shown in Figure 24, in which the most severe condition occurred at the trailing row piles. Based on the calculated shear force profile, the maximum and the minimum shear force occurs at the leading row and the middle row before concrete cracked. However, after the pile cap concrete began cracking around the base of the trailing row, the middle row and the leading row started taking more load because the constraint at the pile head of the trailing rows was affected by the concrete cracking. Subsequently, the load carried by the middle row increases due to the force transferred from the trailing rows after concrete cracked.

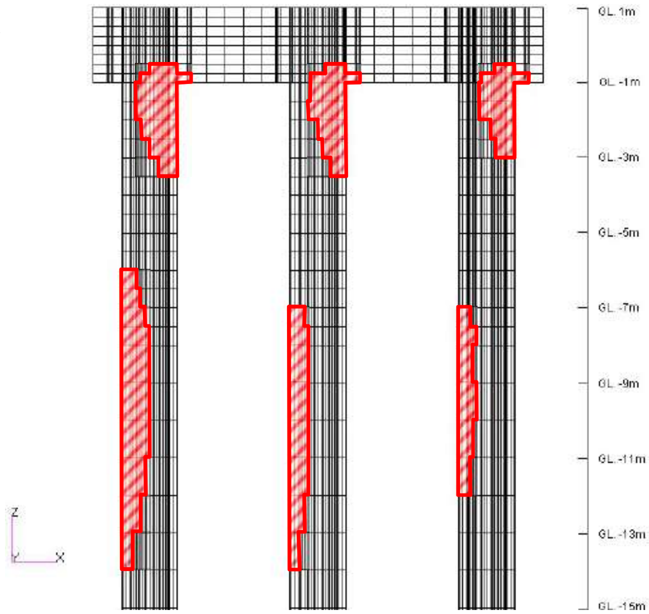

Figure 24 Elevation view of the cracked concrete pattern

Figure 25 gives the comparison between the calculated and the measured rebar stress distribution profile of the piles B6 to B8 under the maximum applied loading. Similar results are also found for the rest of other piles. As shown in the figure, the maximum rebar stress locations coincide with the cracked concrete location given in Figure 24. Unlike the B2 single pile with free head condition shown in Figure 11, the calculated and measured rebar stress is smaller than the yield strength of reinforcement. In addition, the rebar stress profile given in Figure 25 is also different from that of the B2 pile of Figure 11.

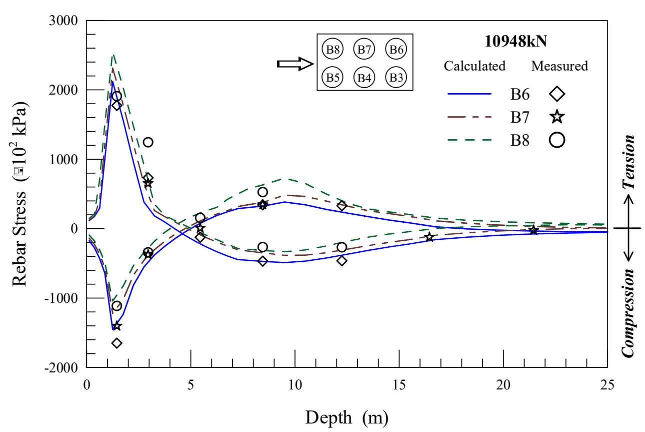

Figure 25 Comparison between the calculated and measured rebar stress

Calculated effects of linear and nonlinear flexural stiffness assumption of pile section on variation of the shear force at pile head, the deflection and moment profile, and the moment curvature relationship are shown in Figures 26, 27, 28 and 29, respectively. As shown in Figures 26, 27 and 28, calculation based on a constant

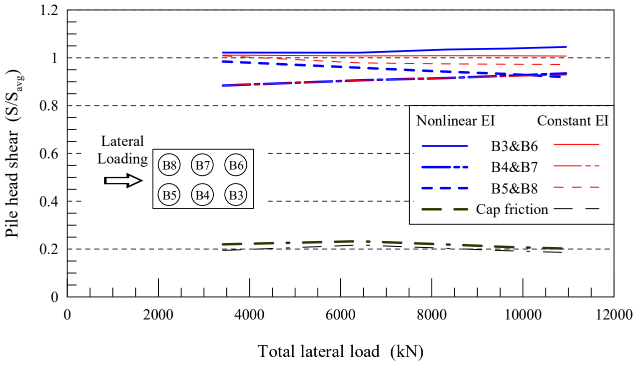

Figure 26 Effect of nonlinear flexural rigidity on the shear forces at group pile head

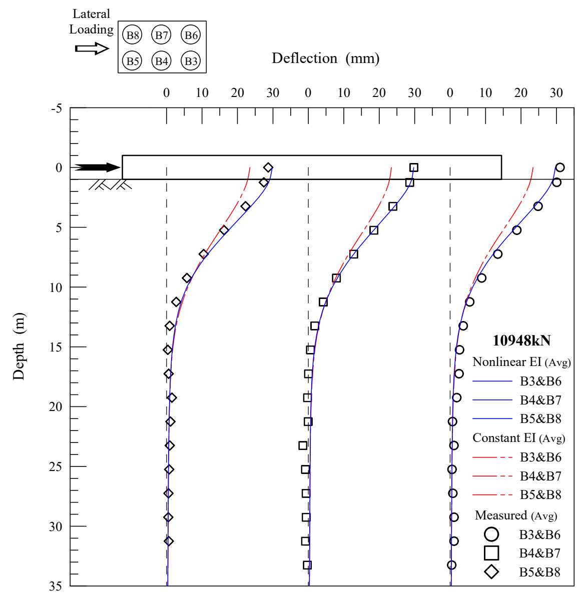

Figure 27 Effect of nonlinear flexural rigidity on calculated deflection profile by each row of piles

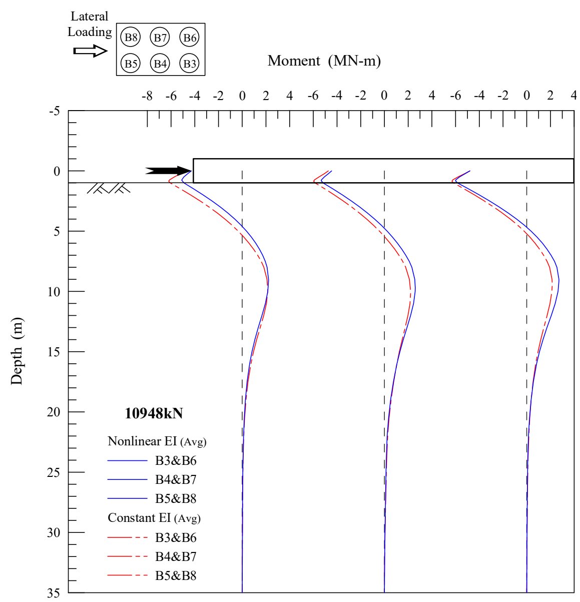

Figure 28 Effect of nonlinear flexural rigidity on calculated moment profile by each row of piles

flexural stiffness assumption tends to under predict the calculated values. On the contrary, a constant pile section flexural stiffness assumption will over predict the moment versus curvature relationship as shown in Figure 29.

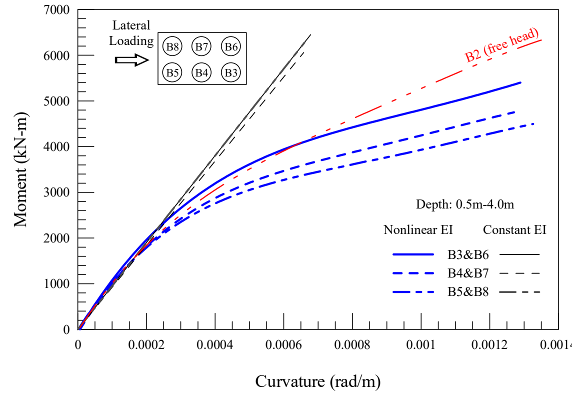

Figure 29 Effect of nonlinear flexural rigidity on the moment-curvature relationship

In Table 4 and Figure 30, under the same displacement, it's defined that the pile group efficiency is the ratio of the average load carried at pile head on each row of pile group to the load at pile head of the B2 single pile, with fixed head condition. In Table 4, SB2F is the load carried at head of the B2 pile with the fixed head condition. Based on the calculation, the leading row and the middle row showed the highest and the lowest efficiency. However, when the applied loading level was higher than 10,000kN, the middle row showed higher efficiency than that of the trailing row piles, possibly resulted from the effect of cracked concrete. To enable comparisons between the test results of the pile group, a calibrated model of the single pile, B2 was developed and used to simulate the response of a single shaft with fixed head condition.

Table 4 Ratio of load carried at each row of piles / single pile with fixed head condition

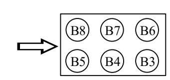

oad (kN)	B2 (fixed) (S_{B2F}, kN)	B5&B8 Avg. (S_{58}, kN)	B5&B8 S_{58}/S_{B2F}	B4&B7 Avg. (S_{47}, kN)	B4&B7 S_{47}/S_{B2F}	B3&B6 Avg. (S_{36}, kN)	B3&B6 S_{36}/S_{B2F}
6416	1662.7	1022.7	0.616	968.6	0.583	1092.1	0.657
8348	2039.2	1310.0	0.642	1273.7	0.625	1438.1	0.706
9643	2317.0	1498.5	0.647	1486.0	0.641	1669.3	0.720
10948	2567.4	1676.5	0.653	1705.5	0.664	1907.6	0.743
Avg.	-	-	**0.640**	-	**0.628**	-	**0.707**

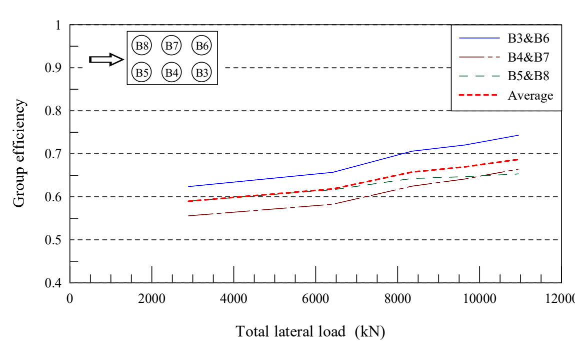

Figure 30 Simulated group efficiency versus total lateral load

The calculated lateral load versus displacement at pile head and the p-y curves along shaft of the B2 pile is shown in Figures 31 and 32, respectively. Significant increasing of the lateral bearing capacity was observed for the fixed head than that of free head condition. The reduced initial modulus of the p-y curves with free head at depth shallower than 7m was observed in Figure 32.

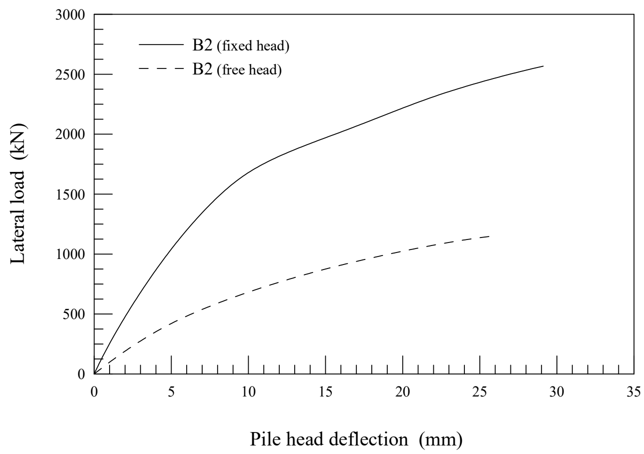

Figure 31 Comparison of load-deflection curves under different head conditions

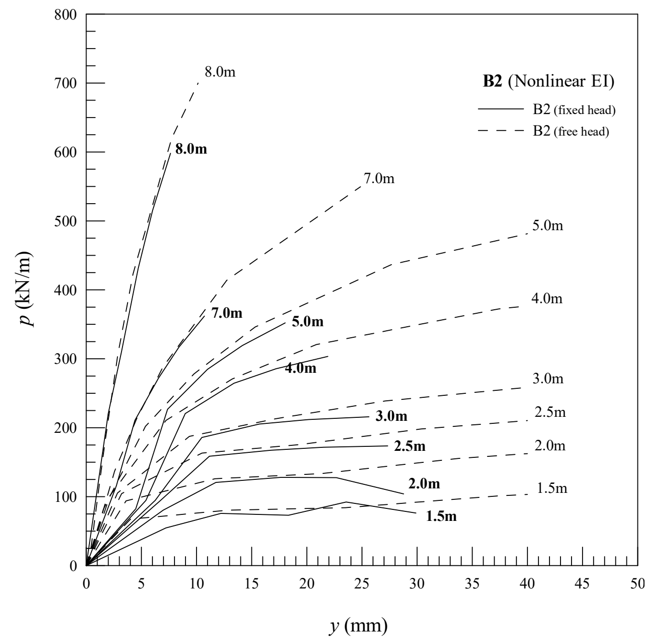

Figure 32 Effect of free and fixed head conditions on the p-y curves of B2 pile

The p-y curves of the pile group are shown in Figure 33, in which the simulated p-y curves of the B2 single pile with fixed head condition are also given for comparison. Based on Figure 33, the p-multiplier of the leading, middle and trailing row piles are 0.867, 0.655 and 0.688, respectively. Study of the same case example using pressuremeter investigation results by Huang et al. (2001) suggested that the p-multiplier of the leading, middle and trailing row piles are 0.93, 0.70 and 0.74, respectively.

4. CONCLUSIONS

Finite element analyses of a pile group were carried out to calibrate a model to the test data and to use the model to evaluate the effects

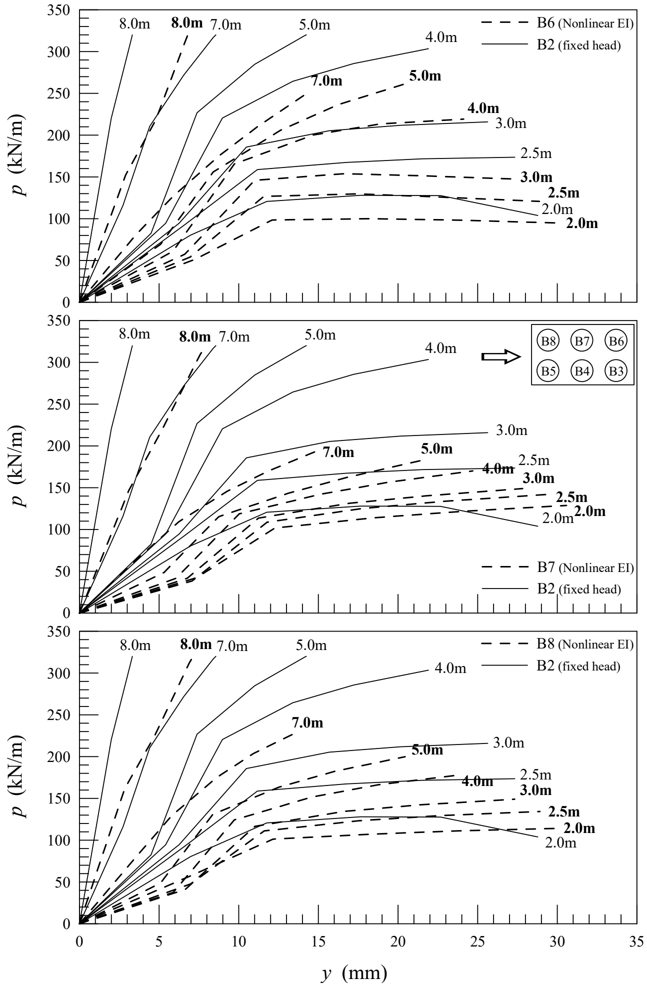

Figure 33 p-y curves of leading, middle and trailing row piles

of concrete cracking. Based on the numerical simulation results, the following conclusions can be drawn:

(1) The free head B2 pile was cracked at the loading level of 630kN and at the respective deflection of 10.1mm. The nonlinear moment curvature relationship of the pile section was highly dependent on distribution of the extensiveness of the cracked concrete area. In addition, calculated results revealed significant differences in the load-deflection response between the fixed and the free head conditions.
(2) Both calculated and measured rebar stress profile of the free head B2 pile showed the maximum tension occurred at depth of 7m. Unlike free head single pile which had only one maximum tension along depth, calculated and measured rebar stress profile of the piles below cap showed the maximum tension occurred at depth of 1.25m and the second larger tension at depth of 9.5m. It helped to explain why the disturbed area of the soil surround a pile in a capped pile group was deeper than that of a single pile with free head.
(3) The leading and the middle row piles in the group carried the highest and the lowest load when the concrete at the pile cap/soil contact area remained its integrity. Increasing the applied loading until concrete cracked, the release of cap constraint due to cracked concrete caused increasing of load carried by the middle row. In general, the load carried by the leading row and the middle row increased with increasing of applied lateral load. On the contrary, the load carried at the trailing row and the frictional resistance at pile cap and ground contact surface decreased with increasing of applied load.

5. ACKNOWLEDGEMENTS

The presented study was carried out as part of a research project funded by the Ministry of Science and Technology (102-2221-E-019 -028 -MY3), Taiwan ROC. The second author is grateful for the financial support.

6. REFERENCES

ACI Committee 318, (1995) Building Code Requirements for Structural Concrete (ACI 318-95) and Commentary (ACI 318R-95), American Concrete Institute.

Bhowmik, S. K., (1992) Three-dimensional nonlinear finite element analysis of laterally loaded piles in clay, Ph.D. Thesis, University of Illinois at Urbana-Champaign.

Brown, D. A., O'Nerill, M. W., Hoit, M., McVay, M., El Naggar, M. H., and Chakraborty, S., (2001) Static and dynamic lateral loading of pile groups, NCHRP Report No. 461, Transportation Research Board, Washington D.C., USA.

Brown, D. A., and Shie, C.-F., (1990) "Three-dimensional finite element model of laterally loaded piles", Computers and Geotechnics, Vol.10, No.1, pp59-79.

Chen, C. H., (1997) Data for planned pile groups tests at Chiayi test site: Workshop report, Department of Civil Engineering, National Taiwan University, Taipei, Taiwan.

Comodromosa, E. M., Papadopouloub, M. C., and Rentzeperis, I. K., (2009) "Pile foundation analysis and design using experimental data and 3-D numerical analysis", Computers and Geotechnics, Vol.36, No.5, pp819-836.

Hibbit, H. D., Karlsson, B. I., and Sorensen, P., (2002) ABAQUS Theory and User's Manual, Version 6.2, Hibbit, Karlsson & Sorensen, Inc., U.S.A.

Hsueh, C. K., Lin, S. S., and Chern, S. G., (2004) "Lateral performance of drilled shaft considering nonlinear soil and structure material behavior", Journal of Marine Science and Technology, Vol.12, No.1, pp62-70.

Huang, A. B., Hsueh, C. K., O'Neill, M. W., Chern, S., and Chen, C., (2001) "Effects of construction on laterally loaded pile groups", Journal of Geotechnical and Geoenvironemntal Engineering, ASCE, Vol.127, No.5, pp385-397.

Lemnitzer, A., Khalili-Tehrani, P., Ahlberg, E. R., Rha, C., Taciroglu, E., Wallace, J. W., and Stewart, J. P., (2010) "Nonlinear efficiency of bored pile group under lateral loading", Journal of Geotechnical and Geoenvironmental Engineering, Vol.136, No.12, pp1673-1685.

Lin, S. S., and Liao, J. C., (2013) "Lateral Load Resistance between Pile-Group and Cap", International Symposium on Advances in Foundation Engineering, Singapore, pp205-210.

Lin, S. S., and Liao, J. C., (2006) "Lateral Response Evaluation of Single Piles Using Inclinometer Data", Journal of Geotechnical and Geoenvironmental Engineering, ASCE, Vol.132, No.12, pp1566-1573.

Lin, S. S., Liao, J. C., Chen, J. T., and Chen, L., (2005) "Lateral Performance of Piles Evaluated via Inclinometer Data", Computers and Geotechnics, Vol.32, No.6, pp411-421.

MacGregor, J. G., (1988) Reinforced Concrete: Mechanics and Design, Prentice Hall, New Jersey, U.S.A.

Mokwa, R. L., and Duncan, J. M., (2003) "Rotational resistance of pile caps during lateral loading", Journal of Geotechnical and Geoenvironmental Engineering, Vol.129, No.9, pp829-837.

Muqtadir, A., and Desai, C. S., (1986) "Three-dimensional analysis of a pile-group foundation", International Journal for Numerical and Analytical Methods in Geomechanics, Vol.10, pp41-58.

Rollins, K. M., and Cole, R. T., (2006) "Cyclic lateral load behavior of a pile cap and backfill", Journal of Geotechnical and Geoenvironmental Engineering, ASCE, Vol.132, No.9, pp1143-1153.

Yang, Z. and Jeremic, B., (2003) "Numerical study of group effects for pile groups in sands", International Journal for Numerical and Analytical Methods in Geomechanics, Vol.27, No.15, pp1255-1276.